Industrial Chemistry & Materials

Accepted Manuscript

This article can be cited before page numbers have been issued, to do this please use: Y. Xu, J. Guo, N. Li, L. Chen, Y. Fang, Q. Cheng, H. Zhang, H. Sun and H. Jiang, *Ind. Chem. Mater.*, 2026, DOI: 10.1039/D6IM00088F.

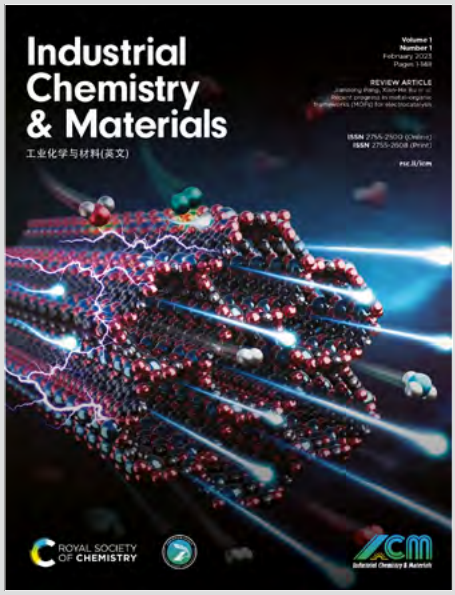

View Article Online
DOI: 10.1039/D6IM00088F

Industrial Chemistry & Materials

View Article Online
DOI: 10.1039/D6IM00088F

ARTICLE

Boron-catalyzed graphitized carbon coating in $Na_4Fe_3(PO_4)_2P_2O_7$ cathodes boosts reaction kinetics for high-rate and long-cycle sodium-ion batteries

Received 00th January 20xx,
Accepted 00th January 20xx

DOI: 10.1039/x0xx00000x

Yuhan Xu,[a] Jinbin Guo,[a] Ningchun Li,[b] Ling Chen,[b] Yaoguo Fang,[d] Qian Cheng,[d] Haoxuan Zhang,*[ab] Hui Sun*[ac] and Hao Jiang*[abc]

Sodium-ion batteries (SIBs) have emerged as a compelling alternative to lithium-ion batteries (LIBs) for large-scale energy storage applications, primarily due to the natural abundance, low cost, and uniform geographic distribution of sodium resources. Among available cathodes, the polyanionic cathode $Na_4Fe_3(PO_4)_2P_2O_7$ (NFPP) combines both excellent cycling stability and a high theoretical capacity. However, the intrinsically low electronic conductivity of NFPP, attributable to the insulating nature of its PO_4-linked FeO_6 units, markedly impedes charge-transfer kinetics. Here, we introduce a boron-assisted carbon coating on NFPP (NFPP/B-C), where boron doping generates p-type carriers and enhances carbon graphitization, increasing the conductivity from 4.76×10^{-4} to 8.4×10^{-4} S cm^{-1}. As a result, the optimized NFPP/B-C cathode delivers an initial charge capacity of 127.2 mAh g^{-1} at 0.1C and 89.2 mAh g^{-1} at 50C, with 91.0 % capacity retention over 10,000 cycles at 20C. These results establish boron-assisted graphitized carbon coatings as an effective strategy for enabling high-power and durable NFPP cathodes for sodium ion batteries.

Keywords: Sodium ion battery; $Na_4Fe_3(PO_4)_2P_2O_7$; Boron doping; Rate capability; Cycling stability.

1 Introduction

Developing cost-effective and durable sodium-ion batteries (SIBs) is essential for accelerating the global transition toward cleaner energy infrastructures and enabling next-generation power systems.[1-4] Especially in energy-storage scenarios with stringent dynamic-response requirements such as grid-frequency regulation, batteries must possess high power density, excellent long-term cycling stability, and high safety.[5,6] The iron-based phosphate $Na_4Fe_3(PO_4)_2P_2O_7$ (NFPP) exhibits remarkable cycling stability and thermal safety due to its stable P-O covalent bonds and minimal lattice volume change during charge and discharge processes.[7] Moreover, NFPP offers a theoretical specific capacity of about 129 mAh g^{-1} and consists of highly abundant, low-cost Fe and P elements, giving it outstanding economic appeal and application prospects for large scale energy storage. However, the FeO_6 octahedra in NFPP are isolated by PO_4 tetrahedra, leading to intrinsically poor electronic conductivity (typically below 10^{-8} S cm^{-1}).[8] This fundamental limitation suppresses charge-transport kinetics and significantly compromises the rate capability, thereby hindering its deployment in power-intensive applications.

Carbon coating is a widely adopted strategy to compensate for their intrinsically low electronic conductivity for polyanionic cathodes.[9] Nevertheless, the typical low-temperature calcination process of NFPP (500°C) results in a relatively low degree of carbon graphitization during pyrolysis, providing limited improvement in electronic transport.[10] To overcome this constraint, many studies introduce highly conductive additives such as reduced graphene oxide or carbon nanotubes to construct multidimensional percolation pathways and accelerate interparticle electron transfer.[11-14] However, these strategies usually require a high total carbon content (>5.0 wt%), which significantly reduces the active-material fraction and electrode

[a] Shanghai Engineering Research Center of Hierarchical Nanomaterials, School of Chemical Engineering, East China University of Science and Technology, Shanghai 200237, China
[b] Key Laboratory for Ultrafine Materials of Ministry of Education, School of Materials Science and Engineering, East China University of Science and Technology, Shanghai, 200237, China
[c] Xinjiang Key Laboratory of Coal Clean Conversion & Chemical Engineering Process, School of Chemical Engineering, Xinjiang University, Urumqi, 830046, Xinjiang, China
[d] Shanghai Xuanyi New Energy Development Co., Ltd, Shanghai 201800, China
Electronic Supplementary Information (ESI) available: [details of any supplementary information available should be included here]. See DOI: 10.1039/x0xx00000x

View Article Online
DOI: 10.1039/D6IM00085E

compaction density, thereby compromising the volumetric energy density. Heteroatoms such as nitrogen, sulfur, and phosphorus can modulate the electronic structure of carbon coatings, thereby enhancing electronic conductivity without the need for large amounts of conductive additives. For example, Han et al. utilized a nitrogen-doped carbon coating derived from polyvinyl pyrrolidone to increase carrier concentration via n-type doping.[15] Yet, such heteroatom doping is often accompanied by the formation of structural defects. Particularly at high operating voltages, nitrogen-doped amorphous carbon can catalyze electrolyte decomposition, aggravating interfacial side reactions and consequently reducing cycling stability.[16-18] Therefore, constructing a highly graphitized carbon coating on NFPP with minimal carbon content (< 2.5 wt%) remains a major challenge for its practical application and industrial development.

In this work, we exploit the low electronegativity of boron, which facilitates strong interactions with oxygen, to construct a B-doped carbon coating on NFPP. Boron doping not only realizes p-type doping and enhances carbon graphitization, which increases the electronic conductivity from 4.76×10^{-4} to 8.4×10^{-4} S cm^{-1}, but also modulates Fe active sites and strengthens Fe-O orbital interactions to stabilize the NFPP lattice structure. The optimized cathode material delivers an initial charge capacity of 127.2 mAh g^{-1} at 0.1C, retains 89.2 mAh g^{-1} at an ultrahigh rate of 50C, and maintains 91.0 % after 10000 cycles at 20C. These outstanding electrochemical performances demonstrate that boron-assisted graphitized carbon engineering constitutes an effective strategy for achieving high-power and long-life NFPP cathodes for sodium ion batteries.

2 Results and discussion

To elucidate the influence of boron doping on the electronic structure of the carbon coating, X-ray photoelectron spectroscopy (XPS) was employed to analyze the bonding configurations. As shown in Fig. 1a, the B 1s spectra identifies four bonding states, corresponding to B_4C, BC_3, BC_2O, and BCO_2 species at progressively higher binding energies.[19] The superior conductivity associated with BC_3 arises from effective p-type doping within the sp^2 carbon network, where boron atoms introduce hole carriers.[20] By contrast, a higher B/C ratio, as in BC_4, favors the formation of localized B-B bonds, which provides limited additional benefit to electrochemical performance. The quantitative distribution of each bonding configuration is summarized in Fig. S1. Accordingly, NFPP/2.4%B-C exhibits the highest BC_3 content, accounting for its optimal electronic conductivity. Consistent with the optimized BC_3 content, NFPP/2.4%B-C also exhibits the highest degree of graphitization, as evidenced by Raman spectra in Fig. 1b. The electronic conductivity of the samples was further evaluated by four-probe measurements. As shown in Fig. 1c, NFPP/2.4%B-C exhibits a pronounced enhancement in electronic conductivity compared with the other samples, which can be attributed to its optimized bonding configuration characterized by the highest BC_3 content.[21] Further insight into the boron-induced structural evolution was obtained from depth-profile XPS analysis. Depth-profile XPS analysis provides additional insight into the surface-subsurface structural evolution of the carbon coating. As shown in Fig. 1d and Table S1, NFPP/2.4%B-C exhibits an increased oxygen content at the surface accompanied by a reduced oxygen concentration in the subsurface region, indicating the formation of a favorable oxygen distribution that preserves an intact sp^2 carbon network for efficient electron transport while maintaining surface functionalities beneficial for interfacial properties.[22-24]

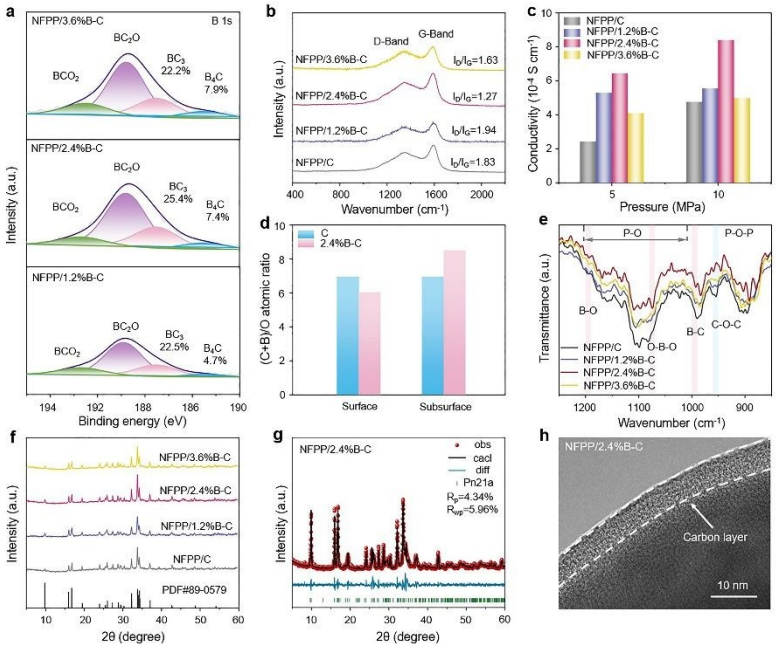

Fig. 1 Characterization of NFPP/B-C samples. (a) B 1s XPS spectra; (b) Raman spectra; (c) electronic conductivity; (d) XPS depth profiles; (e) FTIR spectra; (f) XRD patterns; (g) refined XRD result and (h) high-resolution TEM image.

View Article Online
DOI: 10.1039/D6IM00088B

In the FTIR spectra of the boron-doped samples (Fig. 1e), three distinct bands located at 993.1, 1074.5, and 1194.1 cm^{-1} can be clearly identified, which are assigned to B-C, O-B-O, and B-O vibrational modes, respectively.[25] The enhancement of boron-related vibrational features, accompanied by the attenuation of the C-O-C vibration at 953.5 cm^{-1}, confirms the successful incorporation of boron into the carbon coating. X-ray diffraction (XRD) patterns reveal that all samples crystallize in the orthorhombic Pn21a space group, indicating that boron incorporation does not alter the crystal structure of NFPP (Fig. 1f). Rietveld refinement results (Fig. 1g and Fig. S2) show negligible changes in lattice parameters and unit-cell volume between NFPP/2.4%B-C and pristine NFPP/C, indicating that boron incorporation does not perturb the bulk crystal structure and remains confined to the carbon coating. Detailed refinement results are listed in Table S2. Scanning electron microscopy (SEM) images of the secondary particles (Fig. S3) show that all four samples exhibit comparable particle size distributions. However, upon the addition of excessive boric acid (NFPP/3.6% B-C), a pronounced reduction in particle size is observed, which can be attributed to the mild etching effect of boric acid on the precursor during synthesis. In contrast, NFPP/2.4% B-C maintains well-defined micron-sized secondary spheres assembled from nanoscale primary particles and delivers a tap density of 2.3 g cm^{-3} under a compaction pressure of 220 MPa (Fig. S4). High-magnification TEM image is provided in Fig. 1h to further elucidate the local morphological features, NFPP/2.4%B-C is uniformly coated with an ~8 nm thick carbon layer, which is slightly thicker than that of NFPP/C (~3 nm, Fig. S5). This increase suggests a reduced carbon-layer density, likely resulting from the expansion of closed pores induced by moderate boron doping, which is beneficial for Na^+ insertion/extraction.[26] The steep increase in N_2 adsorption at P/P_0 = 0.05-0.3 observed for 2.4%B-C confirms the above analysis (Fig. S6) .The high-resolution TEM image of NFPP/2.4%B-C shows clear lattice fringes with a crystal plane spacing of 0.27 nm, corresponding to the (424) crystal plane of NFPP (Fig. S7). The EDS element distribution maps indicate that Na, Fe, P, O, C and B elements are uniformly distributed in the sample (Fig. S8).

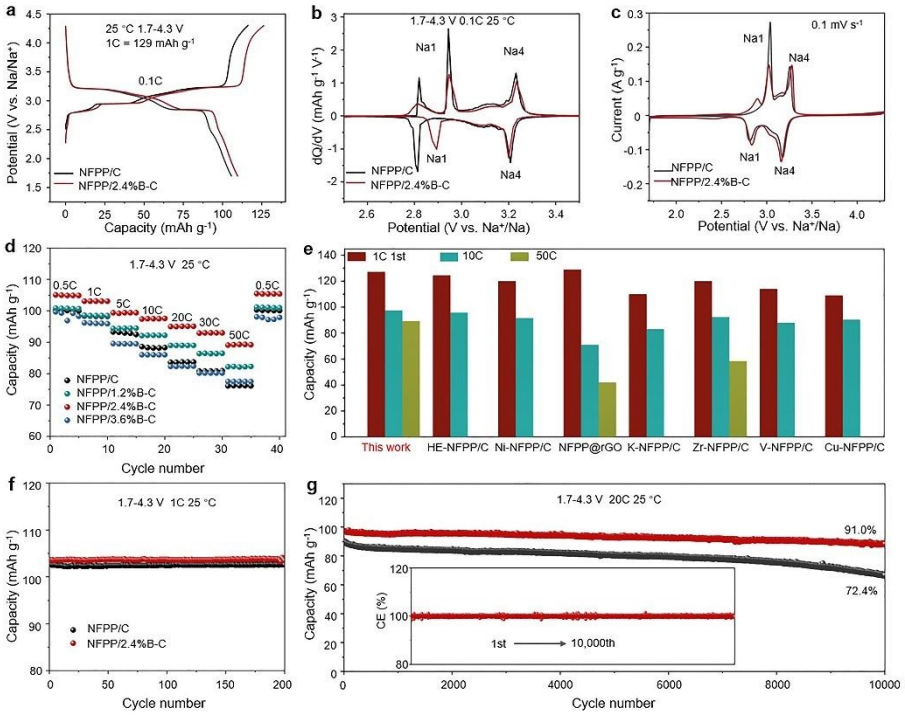

Fig. 2 (a) Initial charge-discharge profiles at 0.1C; (b) the corresponding dQ/dV curves; (c) initial CV curves at 0.1 mV s^{-1}; (d) rate performance at 0.5-50C of NFPP/C and NFPP/2.4%B-C; (e) Comparison of capacities under different current densities with reported work; Cycling performance at (f) 1C and (g) 20C of NFPP/C and NFPP/2.4%B-C.

Coin-type half cells were assembled to evaluate the electrochemical performance of all samples. NFPP/2.4% B-C delivers an initial charge capacity of 127.2 mAh g^{-1} and a discharge capacity of 110.5 mAh g^{-1}, corresponding to a first-cycle Coulombic efficiency of 86.7%. In comparison, pristine NFPP/C exhibits a lower initial charge capacity of 116.2 mAh g^{-1} and a discharge capacity of 105.6 mAh g^{-1}, with a slightly higher first-cycle Coulombic efficiency of 90.9% (Fig. 2a). Differential capacity (dQ/dV) analysis shows that NFPP/2.4% B-C exhibits a reduced polarization of 0.1058 V at the Na1 site compared with 0.1308 V for NFPP/C (Fig. 2b). This reduction in polarization is further confirmed by cyclic voltammetry (CV) at a scan rate of 0.1 mV s^{-1} (Fig. 2c), which indicates lower polarization at both the Na1 and Na4 sites and suggests enhanced electrode reaction kinetics. Rate capability tests reveal that NFPP/2.4% B-C delivers a high discharge capacity of 89.2 mAh g^{-1} at 50C, corresponding to a power density of 12.1 kW kg^{-1} (Fig. 2d, Fig. S9), while maintaining relatively low polarization across the wide rate range of 0.1C-50C (Fig. S10). Compared with literature-reported NFPP-based cathodes, NFPP/2.4% B-C demonstrates competitive rate performance at both 10C and 50C (Fig. 2e).[11, 27-32] Long-term cycling tests show that NFPP/2.4% B-C retains nearly full capacity after 200 cycles at 1C (Fig. 2f). Even after 10000 cycles at 20C, the material maintains a discharge capacity of 88.9 mAh g^{-1} with 91.1% capacity retention, significantly higher than NFPP/C (66.3 mAh g^{-1}) (Fig. 2g). Capacity-decay modeling further

View Article Online DOI: 10.1039/D6IM00088B

predicts that NFPP/2.4% B-C reaches 80% capacity retention after 1733 h of cycling at 20C, compared with 1308 h for NFPP/C (Fig. S11). These results indicate that the enhanced graphitization of the carbon coating effectively mitigates structural stress during prolonged cycling, thereby improving rate performance and long-term cycling stability. To evaluate the practical application potential, we assembled coin-type full cells with hard carbon (HC) as the anode. As shown in Fig. S12, the discharge specific capacities of NFPP/2.4%B-C//HC at 0.5C, 1C, 2C, 5C, and 10C are 105.9, 101.9, 96.4, 81.5, and 68.3 mAh g^{-1}, respectively, which are higher than those of NFPP/C//HC (96.0, 92.8, 86.6, 68.9, and 53.7 mAh g^{-1}). Furthermore, NFPP/2.4%B-C//HC retains a capacity of 102.6 mAh g^{-1}after 500 cycles at 1C, with a capacity retention of 97.8%.

To comprehensively probe the Na^+ transport kinetics across the cathode electrolyte interphase (CEI) and the interfacial charge-transfer process, temperature-dependent electrochemical impedance spectroscopy (EIS) measurements were carried out in the temperature range of 0-50°C, and the corresponding activation energies were derived based on the Arrhenius formalism.[33] As shown in Fig. 3a, NFPP/2.4%B-C exhibits a markedly attenuated temperature dependence of the charge-transfer resistance (Rct) relative to NFPP/C, giving rise to a lower activation energy of 43.31 kJ mol^{-1}, as opposed to 46.66 kJ mol^{-1} for the NFPP/C. The reduced energy barrier implies more favorable Na^+ transport kinetics within the NFPP bulk. A similar trend is observed for the surface film resistance (Rsf). The activation energies associated with Rsf are calculated to be 26.31 kJ mol^{-1} for NFPP/C and 20.70 kJ mol^{-1} for NFPP/2.4%B-C, respectively (Fig. 3b), indicating facilitated Na+ migration across the CEI layer in the NFPP/2.4%B-C cathode. The EIS spectra and the corresponding distribution of relaxation times (DRT) analyses for NFPP and NFPP/2.4%B-C are shown in Fig. 3c and 3d. DRT analysis was employed to decouple the contributions of different electrochemical processes by resolving the characteristic peaks at distinct time constants.[34] As the charging voltage increases beyond 3.1 V, the cathode-electrolyte interfacial impedance of both electrodes decreases, with Rct exhibiting an initial decline followed by a slight increase. Throughout the charging process, NFPP/2.4%B-C consistently exhibits lower Rct values than NFPP/C. Moreover, at the end of charging, the diffusion-related impedance of NFPP/2.4%B-C is notably smaller, confirming significantly enhanced Na^+ diffusion kinetics.

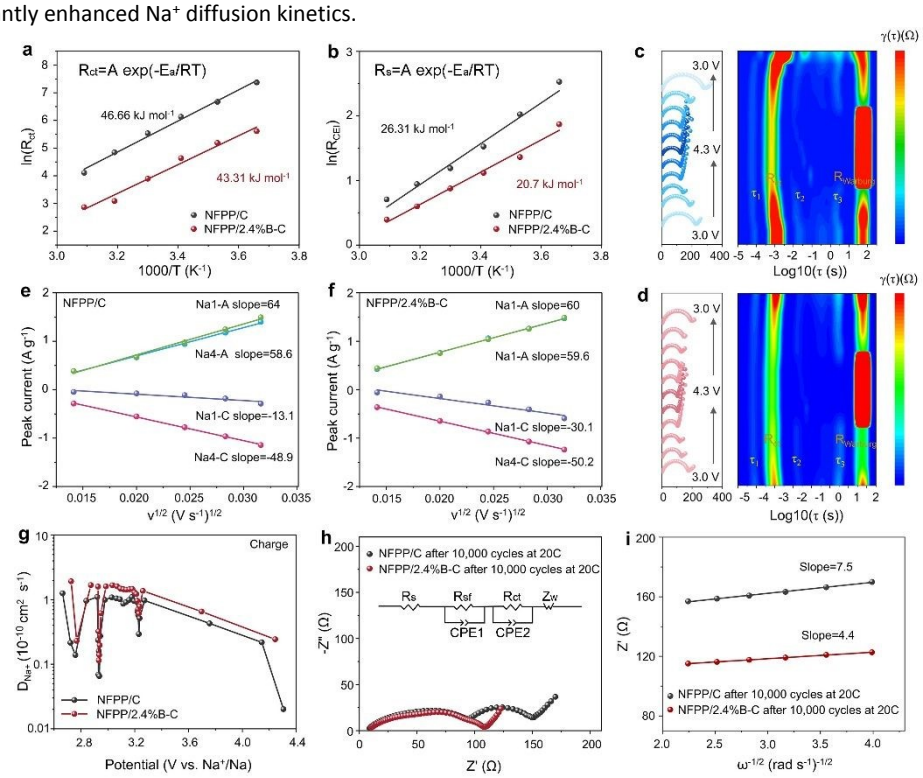

Fig. 3 (a, b) The calculated activation energies of Na-ion diffusion within the interface charge transfer and CEI film; (c, d) in-situ EIS spectra and the corresponding DRT contour plots; (e, f) slopes analysis of i_p *vs*. $v^{1/2}$ and (g) Na-ion diffusion coefficient calculated by GITT of NFPP/C and NFPP/2.4%B-C; (h) EIS spectra and (i) linear fitting of Z' *vs*. $\omega^{-1/2}$ of NFPP/C and NFPP/2.4%B-C after 10000 cycles at 20C.

Based on the cyclic voltammetry (CV) results (Fig. S13), a linear relationship was fitted between the peak current (ip) and the square root of the scan rate ($v^{1/2}$) for the Na1 and Na4 redox couples (Fig. 3e and 3f). Notably, the slopes corresponding to the respective peaks of the NFPP/2.4%B-C composite are the largest, which confirms that this material possesses superior Na-ion diffusion kinetics. In addition, GITT measurements also reveal that NFPP/2.4%B-C has a higher Na-ion diffusion coefficient than NFPP/C over all tested voltage ranges (Fig. 3g). To further evaluate the kinetic stability of the samples upon long-term cycling, EIS measurements were conducted after 10,000 cycles at 20C (Fig. 3h). After cycling, the Rsf and Rct values of NFPP/C increased significantly, accompanied by a distinct enlargement of the R_{sf} semicircle. This suggests that NFPP/C underwent more severe side reactions (e.g., electrolyte decomposition) during the late cycling stage, which induced continuous formation and rupture of the CEI film. From the linear fitting in the Warburg

View Article Online
DOI: 10.1039/D6IM00088E

region of the EIS spectra, the slope of Z' versus $\omega^{1/2}$, known as the Warburg factor σ, is varies inversely with the sodium ion diffusion coefficient(Fig. 3i).The slope for NFPP/2.4%B-C (4.4) is smaller than that for NFPP/C (7.5), indicating that the modified material maintains lower ionic diffusion resistance and enables faster sodium ion migration even after extended cycling.

To elucidate the origin of the enhanced electrochemical performance, density functional theory (DFT) calculations were performed to provide mechanistic understanding. Differential charge density maps (Fig. 4a) indicate pronounced electron redistribution upon boron incorporation, where charge transfer from the delocalized π system to localized σ bonds induces hole generation in the boron-doped carbon, giving rise to p-type conductivity and improved electronic transport. Among the examined configurations, the BC_3 structure exhibits the highest hole density, consistent with its superior conductivity compared with BC_2O and BCO_2. The effect of boron doping on the electronic structure was further examined by density of states (DOS) analysis. As shown in Fig. 4b and 4c, boron incorporation significantly narrows the band gap of NFPP, facilitating charge carrier transport and enhancing overall electronic conductivity. In addition, based on d-band center theory, the bonding characteristics of Fe were analyzed.[35,36] The Fe 3d partial density of states (pDOS) (Fig. 4d) reveal that the d-band center of NFPP/2.4% B-C shifts upward from -4.12 eV to -3.45 eV relative to NFPP/C, accompanied by bonding Fe-O states located closer to the Fermi level. This shift indicates strengthened Fe-O interactions, originating from enhanced electronic coupling between the boron-doped carbon layer and NFPP, which promotes electron occupation in Fe-O bonding states and stabilizes the local bonding environment (Fig. 4e). Furthermore, Na^+ migration calculations demonstrate that NFPP/2.4% B-C possesses a substantially lower diffusion energy barrier than NFPP/C (Fig. 4f and 4g), suggesting accelerated Na^+ transport kinetics. Such enhanced ion diffusion not only contributes to improved rate performance but also mitigates stress accumulation during repeated cycling, thereby supporting long-term cycling stability.

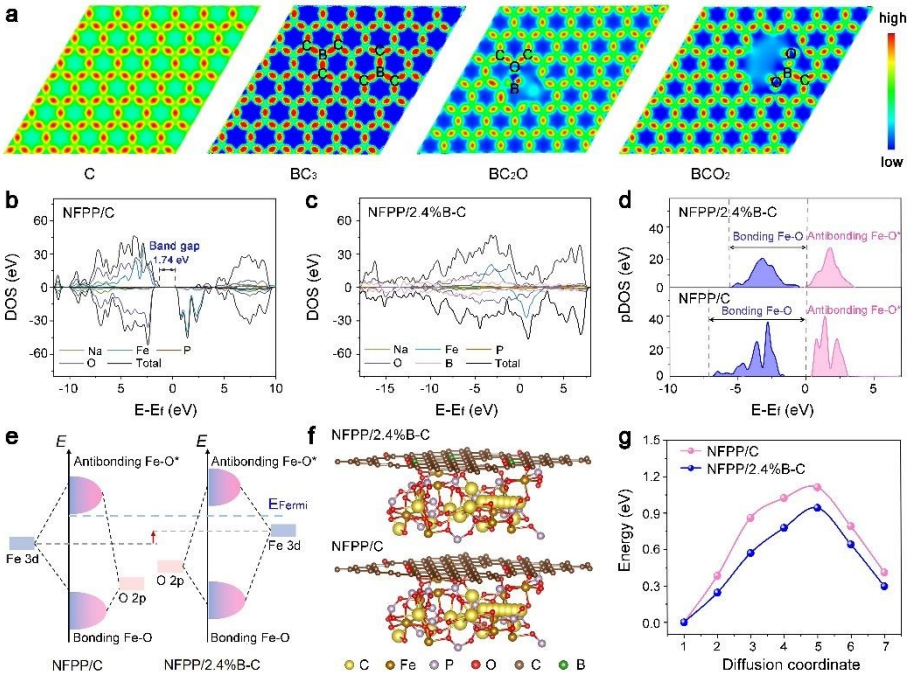

Fig. 4 (a) Differential charge density of C, BC_3, BC_2O and BCO_2; Calculated (b, c) total and (d) partial density of states analysis of NFPP/C and NFPP/2.4%B-C; (e) Schematic of the energy band structural regulation; (f) Migration path of Na^+ and (g) corresponding Na^+ migration energy barriers of NFPP/C and NFPP/2.4%B-C.

3 Conclusions

In summary, we report a boron-assisted graphitized carbon coating strategy to effectively overcome the intrinsically poor electronic conductivity of the polyanionic NFPP cathode for sodium-ion batteries. Benefiting from boron induced p-type charge carriers and an enhanced degree of carbon graphitization, the electronic conductivity of NFPP is substantially improved, which markedly accelerates charge transfer kinetics and enables efficient high-rate sodium storage. As a result, the optimized NFPP/B-C cathode delivers high reversible capacity at both low and ultra-high rates, together with exceptional cycling stability over prolonged operation. This work not only elucidates the critical role of heteroatom engineered carbon coatings in regulating electronic transport of polyanionic cathodes, but also provides a scalable and effective design principle for developing high-power and long-life sodium-ion battery cathode materials.

4 Experimental section

4.1 Materials synthesis

View Article Online
DOI: 10.1039/D6IM00086F

NFPP/C composites were synthesized according to the designed Na:Fe:P molar ratio of 4:3:4. Na_2CO_3 and a ferric pyrophosphate precursor (F2P-A001, Zhongwei Co., Ltd) were weighed to give a total mass of 65 g. Glucose (7 wt%) and PEG-400 (3 wt%) were added as the carbon source and dispersant, followed by an appropriate amount of H_3BO_3. The mixture was dispersed in 500 mL of deionized water and milled at 800 r min^{-1} for 5 h, after which the slurry was spray-dried to obtain the precursor powder. Calcination was then carried out under flowing N_2 by heating to 550 °C at 5 °C min^{-1} and holding for 10 h to obtain the final NFPP/C materials. According to the theoretical boron content in the carbon coating, the products are denoted as NFPP/1.2%B-C, NFPP/2.4%B-C, and NFPP/3.6%B-C.

4.2 Materials characterizations

Morphology analysis was performed using: scanning electron microscopy (SEM, Hitachi, S-4800) for surface features, high-resolution transmission electron microscopy (HRTEM, FEI Talos F200X) for internal structures. Compacted density was measured by Compaction Density Tester (IEST, PRCD3100). Characterizing crystal structure by X-ray diffraction (XRD, Bruker, D8 Advance). The corresponding lattice parameters were obtained from Rietveld refinement using the GSAS software. Characterizing surface chemistry by X-ray photoelectron spectroscopy (XPS, Thermo Fisher Scientific, K-Alpha). For XPS depth profiling, argon ion sputtering was employed with an etching depth of 1 nm. Structural features were further tested via Fourier transform infrared spectroscopy (FTIR, Thermo IS20). The degree of graphitization was evaluated via Raman spectroscopy (Thermo Fisher Scientific, DXR3xi). Carbon content was precisely measured using an elemental analyzer (Vario El Cube). Electronic conductivity was measured using four-point probe resistance tester (RTS-9 type).

4.3 Electrochemical measurements

Active material (0.24 g), N-methyl-2-pyrrolidone (NMP, 0.8 g), Super P (0.03 g), and polyvinylidene fluoride (PVDF, 0.03g) were well mixed to form a homogeneous slurry. The slurry was then coated onto carbon-coated aluminum foil and dried at 120 °C under vacuum for 12 hours. The areal density of each electrode sheet is nearly 1.8 mg cm^{-2}. Electrolyte composition: 1.0 M $NaClO_4$, EC/ DEC (1:1), and 5 wt% FEC. Na metal anodes and glass fiber separator were used to assemble CR2032 cells in a glovebox (Ar atmosphere). Galvanostatic charge-discharge cycling and galvanostatic intermittent titration technique (GITT) were evaluated on a LAND-CT2001A system (1.7-4.3 V vs. Na^+/Na, 1C = 129 mA g^{-1}). Cyclic voltammetry (CV, 1.7-4.3 V) and Electrochemical impedance spectroscopy (EIS, 0.1-100 kHz) measurements were conducted on electrochemical workstation (Autolab, PGSTAT302N). MATLAB was utilized to derive distribution of relaxation times (DRT).
The formula for calculating the diffusion coefficient based on GITT:

$$D^{\mathrm{GITT}} = \frac{4}{\pi\tau}\left(\frac{m_{\mathrm{B}}V_{\mathrm{M}}}{M_{\mathrm{B}}S}\right)^2 \quad (1)$$

where τ, m_B, V_M, M_B, and S represent constant-current pulse duration (s), active material mass (g), molar volume (cm^3 mol^{-1}), molar mass (g mol^{-1}), and electrode area (cm^2).

The lifetime prediction of the material was performed using the capacity fade model established by J. R. Dahn. The core mathematical expression of this model is as follows:

$$Q_d(t) = Q_0(1 - A\sqrt{t}) - \frac{1}{2}\left(\left|\frac{dQ}{dV}\right|_L + \left|\frac{dQ}{dV}\right|_U\right) \times (\Delta V(t) - \Delta V_0) \quad (2)$$

where $Q_d(t)$ is capacity at t time, and Q_0 is the initial capacity. $\left(\left|\frac{dQ}{dV}\right|_L \text{ and } \left|\frac{dQ}{dV}\right|_U\right)$ represent the absolute values of the derivative of capacity with respect to voltage at the lower and upper cutoff voltages, respectively, during a 0.1C charging process. ΔV_0 is the value of the first cycle.

The slope of peak current (Ip) *vs*. scan rate's square root ($v^{1/2}$) is positively correlated with the Na^+ diffusion rate according to the Randles-Sevcik equation.

$$I_p = 2.69\times10^5 n^{\frac{3}{2}} A D_{Na^+}^{\frac{1}{2}} C v^{\frac{1}{2}} \quad (3)$$

Where *n*, *A*, *C*, and *v* are electron transfer number, cathode area (cm^2), Na+ concentration (mol cm^{-3}), scan rate (V s^{-1}), respectively.

4.4 DFT calculation

Density functional theory (DFT) calculations were performed using the projector-augmented wave (PAW) method. The carbon coating is represented as a periodic carbon layer. The exchange-correlation effects were treated within the generalized gradient approximation (GGA) using the Perdew-Burke-Ernzerhof (PBE) functional. The GGA+U method was employed to better describe the localized electronic states of the transition metals. The U value was 4.0 eV for Fe. A plane-wave basis set with a cutoff energy of 450 eV was employed. During structural optimizations, the total energy and atomic forces were

converged to 10^{-5} eV and 0.02 eV $Å^{-1}$, respectively. To avoid interactions between periodic images, a vacuum layer of 15 Å was introduced along the c-axis.

View Article Online
DOI: 10.1039/D6IM00088F

Author contributions

Yuhan Xu: Conceptualization; investigation; data curation; methodology; writing original draft. Jinbin Guo: Resources; software; validation. Ningchun Li: Investigation; methodology; visualization; formal analysis. Ling Chen: Methodology; writing-review & editing; funding acquisition. Yaoguo Fang: Methodology; conceptualization. Qian Cheng: Methodology; formal analysis. Haoxuan Zhang: Methodology; formal analysis; visualization; supervision; writing-review and editing. Hui Sun: Conceptualization; supervision; writing-review and editing. Hao Jiang: Methodology; supervision; writing-review & editing; supervision; funding acquisition.

Conflicts of interest

The authors declare no conflict of interest.

Acknowledgements

This work was supported by the Shanghai Pilot Program for Basic Research (22TQ1400100-13), the Key Research and Development Program of Xinjiang Uygur Autonomous Region (2024B01018), and the Tianshan Talent Research Science and Technology Innovation Team of Xinjiang Uygur Autonomous Region (2024TSYCTD0004).

References

1. Z. H. Cui, C. Liu and A. Manthiram, A perspective on pathways toward commercial sodium-ion batteries, *Adv. Mater.*, 2025, **37**, 2420463.
2. H. S. Hirsh, Y. X. Li, D. H. S. Tan, M. H. Zhang, E. Y. Zhao E and Y. S. Meng, Sodium-ion batteries paving the way for grid energy storage, *Adv. Energy Mater.*, 2020, **10**, 2070134.
3. T. Jin, H. X. Li, K. J. Zhu, P. F. Wang, P. Liu and L. F. Jiao, Polyanion-type cathode materials for sodium-ion batteries, *Chem. Soc. Rev.*, 2020, **49**, 2342-2377.
4. W. B. Li, C. T. Zhao, C. Yu, Y. Ju, J. Q. Huang, Y. Y. Lu, H. Jiang, S. Gu, Z. G. Lu, X. Yang, L. Yu, Y. Ren, S. Q. Shi and W. H. Chen, Advanced batteries for sustainable energy storage, *Green Energy Environ.*, 2025, **10**, 2201-2258.
5.Y. Chen, G. J. Zhao, J. Y. Dong, J. Wang, D. X. Dong, Z. Li, M. X. Zhao, Z. J. Shi and Z. H. Niu, Green recovery of all-solid-state sodium-ion batteries/lithium-ion batteries by ionic liquids, deep eutectic solvents and low-melting mixture solvents, *Ind. Chem. Mater.*, 2025, **3**, 464-474.
6. J. X. Yu, L. Chen, H. F. Yu, H. J. Zhang, Q. L. Cheng and H. Jiang, Modulating oxygen anion microenvironment of P2-type cathodes enables long-term cycling stability for high-voltage sodium-ion batteries, *Green Energy Environ.*, 2026, DOI: 10.1016/j.gee.2026.04.005.
7. H. J. Xia H, W. C. Xu, W. G. Wang, H. Wu, Y. Zhang, W. L. Cai and K. P Wu, $Na_4Fe_3(PO_4)_2P_2O_7$ cathode for sodium-ion batteries: Critical technologies and progress from fundamental advances to industrialization challenges, *Energy Storage Mater.*, 2026, **84**, 104788.
8. L. L. Zhou, H. F. Yu, B. Zhou, J. X. Yu, L. Chen and H. Jiang, Dual-carbon-coated $Na_2FeP_2O_7$ cathode materials for Na-ion batteries with superior high-rate and cycling stability, *Adv. Energy Sustain. Res.*, 2024, **5**, 2400120.
9. C. Liu, Z. Zhang, H. Y. Liao, Y. M. Jiang, Z. X. Li and Y. H. Gao, Unlocking the potential: $Na_4Fe_3(PO_4)_2P_2O_7$ supporting the innovation of commercial sodium-ion batteries, *Adv. Funct. Mater.*, 2025, **35**, 2424759.
10. N. C. Li, C. W. Li, M. Sedlačík, P. Saha, Q. L. Cheng, H. F. Yu and H. Jiang, Modulating electronic structure to expedite $Na_4Fe_3(PO_4)_2P_2O_7$ reaction kinetics for high-power Na-ion batteries, *Rare Metals*, 2025, **44**, 8444-8452.
11. T. C. Yuan, Y. X. Wang, J. X. Zhang, X. J. Pu, X. P. Ai, Z. X. Chen, H. X. Yang and Y.L. Cao, 3D graphene decorated $Na_4Fe_3(PO_4)_2(P_2O_7)$ microspheres as low-cost and high-performance cathode materials for sodium-ion batteries, *Nano Energy*, 2019, **56**, 160-168.
12. J. Ni, W. J. Chen, X. Y. Zhang, H. Xu, M. H. Zhang and X. L. Wu, Nitrogen doped hierarchical porous carbon for supercapacitors and zinc ion hybrid capacitors, *Ind. Chem. Mater.*, 2025, **3**, 475-484.
13. J. H. Zhang, L. B. Tang, Y. Zhang, X. Q. Li, Q. J. Xu, H. M. Liu and Z. F. Ma, Polyvinylpyrrolidone assisted synthesized ultra-small $Na_4Fe_3(PO_4)_2P_2O_7$ particles embedded in 1D carbon nanoribbons with enhanced room and low temperature sodium storage performance, *J. Power Sources*, 2021, **498**, 229907.
14. X. P. Li, Y. Meng and D. Xiao, Three-dimensional holey graphene modified $Na_4Fe_3(PO_4)_2P_2O_7$/C as a high-performance cathode for rechargeable sodium-ion batteries, *Chem. Eur. J.*, 2023, **29**, 202203381.
15. F. Han, M. Li, X. D. Miao, J. H. Li, X. J. Yin and N. Q. Zhang, Mechanochemical strategy of N-doped carbon-armored $Na_4Fe_3(PO_4)_2P_2O_7$ cathodes for sodium-ion batteries, *Electrochim. Acta*, 2025, **540**, 147218.
16. Y. Jiang, N. Xiao, K. Yu and J. S. Qiu, N-doped porous graphite-like carbon armored with dense amorphous shell through a Trojan horse strategy for high performance potassium-ion battery anode, *Small*, 2025, **21**, e07641.
17. Y. Li, M. Q. Liu, X. Feng, Y. Li, F. Wu, Y. Bai and C. Wu, How can the electrode influence the formation of the solid electrolyte interface?, *ACS Energy Lett.*, 2021, **6**, 3307-3320.
18. J. H. Wee, C. H. Kim, T. Tojo, G. C. Choi, C. M. Yang and Y. A. Kim. Boron-doped edges as active sites for water adsorption in activated carbons, *Langmuir*, 2021, **37**, 13179-13186.
19. C. Wang, Z. Y.Guo, W. Shen, Q. J. Xu, H. M. Liu and Y. G. Wang, B-doped carbon coating improves the electrochemical performance of electrode materials for Li-ion batteries, *Adv. Funct. Mater.*, 2014, **24**, 5511-5521.

View Article Online
DOI: 10.1039/D6IM00088F

20. S. Sarkar, R. Roy, B. K. Das and K. K. Chattopadhyay, Temperature-dependent site selection of boron doping in chemically derived graphene, *Carbon*, 2021, **184**, 253-265.
21. D. Liu, Z. F. Wang, H. Jia, Z. L. Yi, L. J. Xie, Z. C. Tao, X. Yan, D. Jiang, K. G. Fang, Q. Q. Kong and C. M. Chen, Whole landscape of evolution and removal of boron catalytic graphitization of graphene for thermal management and electromagnetic interference shielding, *Appl. Surf. Sci.*, 2025, **695**, 162631.
22. G. P. Yin, Y. Z. Gao, P. F. Shi, X. Q. Cheng and A. Aramata, The effect of boron doping on lithium intercalation performance of boron-doped carbon materials, *Mater. Chem. Phys.*, 2003, **80**, 94-101.
23. S. L. Ding, S. J. Zheng, M. J. Xie, L. M. Peng, X. F. Guo and W. P. Ding, One-pot synthesis of boron-doped mesoporous carbon with boric acid as a multifunction reagent, *Micropor. Mesopor. Mater.*, 2011, **142**, 609-613.
24. H. N. Murty, D. L. Biederman and E. A. Heintz, Apparent catalysis of graphitization. 3. Effect of boron, *Fuel*, 1977, **56**, 305-312.
25. Y. A. Wang, Y. L. Sui, Z. Xiao, W. B. Fei, M. T. Deng, X. P. Zhang, H. Z. Guo, R. H. Wang and L. Wu, Inner/interface engineered iron/manganese-based mixed phosphate cathode with high energy density and ultra-long cycle life for sodium-ion batteries, *Adv. Funct. Mater.*, 2025, **35**, 2500290.
26. P. Zheng, W. Zhou, Y. Mo, B. Zheng, M. M. Han, Q. Zhong, W. W. Yang, P. Gao, L. Z. Yang and J. L. Liu, Multi boron-doping effects in hard carbon toward enhanced sodium ion storage, *J. Energy Chem.*, 2025, **100**, 730-738.
27. P. Y. Dong, F. Peng, Q. M. Zhang Q, H. Wang, Y. Q. Chu, C. D. Chen and C. H. Yang, High entropy boosts the low temperature Na^+-storage performance of $Na_4Fe_3(PO_4)_2P_2O_7$, *Angew. Chem. Int. Ed.*, 2025, **64**, e202502693.
28. X. R. Qi, H. H. Dong, H. Yan, B. X. Hou, H. Y. Liu, N. Z. Shang, L. G. Wang, J. J. Song, S. Q. Chen, S. L. Chou and X. X. Zhao, Hollow core-shelled $Na_4Fe_{2.4}Ni_{0.6}(PO_4)_2P_2O_7$ with tiny-void space capable fast-charge and low-temperature sodium storage, *Angew. Chem. Int. Ed.*, 2024, **63**, e202410590.
29. X. L. Wu, Y. Cui, Y. M. Yao Y, Y. L. Gao, C. L. Guo, W. K. Zhang, M. Q. Guo, Z. L. Yi, S. Q. Shi and H. Chen, Effect of K^+-doping on oxygen vacancies reduction, kinetics and cycling stability of $Na_4Fe_3(PO_4)_2P_2O_7$/C cathodes for sodium-ion batteries, *J. Energy Storage*, 2025, **132**, 117661.
30. H. M. Dai, Z. A. Yang, T. T. Xie, Z. H. Zhao, Y. F. Shang, C. C. Ai and Q. Yi, Zirconium modification induced small-polaron breakdown in $Na_4Fe_3(PO_4)_2P_2O_7$ as superior cathode in sodium-ion battery, *Adv. Funct. Mater.*, 2025, **35**, 2505185.
31. S. J. Xu, J. S. Yuan, D. H. Ma, L. L. Dai, T. T. Gan, X. S. Zhang, X. L. Peng, X. X. Zuo, J. Gao and X. Y. Gao, Hollow spherical $Na_{3.95}Fe_{2.95}V_{0.05}(PO_4)_2P_2O_7$ suppressing inactive Maricite-$NaFePO_4$ with ultrahigh dynamics performance, *Nano Energy*, 2024, **132**, 110404.
32. X. R. Qi, Q. Y. Dong, H. H. Dong, B. X. Hou, H. Y. Liu, N. Z. Shang, S. H. Zhang, L. G. Wang, H. Shao, Y. B. Shen, S. Q. Chen and X. X. Zhao, Copper-induced lattice distortion in $Na_4Fe_3(PO_4)_2(P_2O_7)$ cathode enabling high power density Na-ion batteries with good cycling stability, *Energy Storage Mater.*, 2024, **73**, 103861.
33. H. F. Yu, Z. F. Yang, Q. Han, L. Chen, H. Jiang and C. Z. Li, Operando building of a superior interface hybrid film enables chemo mechanically durable Co-free Ni-rich cathodes, *ACS Nano*, 2024, **18**, 13428-13436.
34. L. L. Zhou, H. F. Yu, C. W. Li, L. Chen L and H. Jiang, Mitigating lattice distortion of $Na_4Fe_3(PO_4)_2P_2O_7$ cathodes at high voltage for high-capacity Na-ion batteries; *ACS Sustain. Chem. Eng.*, 2025, **13**, 4908-4915.
35. Z. P. Wang, J. H. Huang, L. Wang, Y. Y. Liu, W. H. Liu, S. L. Zhao and Z. Q. Liu, Cation-tuning induced d-band center modulation on Co-based spinel oxide for oxygen reduction/evolution reaction, *Angew. Chem. Int. Ed.*, 2022, **61**, e202114696.
36. K. Jia, J. Ma, J. X. Wang, Z. Liang, G. J. Ji, Z. H. Piao. R. H. Gao, Y. F. Zhu, Z. F. Zhuang, G. M. Zhou and H. M. Cheng, Long-life regenerated $LiFePO_4$ from spent cathode by elevating the d-band center of Fe, *Adv. Mater.*, 2023, **35**, 2208034.

View Article Online
DOI: 10.1039/D6IM00088F

The data that support the findings of this study are available from the corresponding author upon reasonable request.

Supplementary information (SI) is available. See DOI:XXX